

Electromagnetic Models for Passive Detection and Localization of Multiple Bodies

Vittorio Rampa¹, Member, IEEE, Gian Guido Gentili², Stefano Savazzi³, Member, IEEE,
and Michele D'Amico⁴, Senior Member, IEEE

Abstract—This article proposes a multibody electromagnetic (EM) model for the quantitative evaluation of the influence of multiple human bodies in the surroundings of a radio link. Modeling of human-induced fading is the key element for the development of real-time device-free (or passive) localization (DFL) and human presence-aware systems (HPS) based on the processing of the received signal strength (RSS) data recorded by radio frequency devices. The proposed physical–statistical model is able to relate the RSS measurements to the position, size, orientation, and random movements of people located in the link area. This novel EM model is thus instrumental for crowdsensing, occupancy estimation, and people counting applications for indoor and outdoor scenarios. This article presents the complete framework for the generic N-body scenario where the proposed EM model is based on the knife-edge approach that is generalized here for multiple targets. The EM-equivalent size of each target is then optimized to reproduce the body-induced alterations of the free-space radio propagation. The predicted results are then compared against the full EM simulations obtained with a commercially available simulator. Finally, experiments are carried out to confirm the validity of the proposed model using IEEE 802.15.4-compliant industrial radio devices.

Index Terms—Electromagnetic (EM) body model, radio propagation, scalar diffraction, wireless sensor networks.

I. INTRODUCTION

HUMAN presence-aware systems (HPSs) are rapidly growing as new services become available in various areas of modern life [1], such as assisted living, ambient intelligence, smart spaces, home automation, human–robot collaboration, safety, and security, just to cite a few. Among these applications, noncooperative, also known as passive, HPS is the most attractive since it does not require the monitored users to carry or wear any electronic device or specific

sensors. Usually, these systems are vision-based [2]–[4]; however, the ubiquitous presence of wireless networks paves the way toward the exploitation of wireless radio frequency (RF) networks, not only as communication devices but also as body proximity/location virtual sensors. Last but not least, radio-based HPS are privacy-neutral since they do not reveal any privacy information about the monitored people.

HPS systems exploit the fact that people, or obstacles, in the surroundings of an area covered by a wireless radio network induce signal alterations that can be detected and exploited for body occupancy inference applications. For instance, device-free localization (DFL) systems [5], [6] exploit a network of RF nodes to detect the presence, to locate and track the position of moving objects or people in a confined area covered by the wireless network itself. However, a radio-based HPS is not only able to localize and track [7]–[10] people, or objects, but it has also been proven to efficiently perform other tasks such as to count the number of people [11], to identify and recognize patterns related to their activities [12], [13] and intentions [12], to detect dangerous worker conditions and safety status [14], [15], and to act as a proximity monitor [16]. This is made possible as the presence of targets (i.e., objects or people) affects the propagation of the radio waves in the covered area [17], [18], for example, by inducing predictable alterations of the received signal strength (RSS) field that depend on the targets position, in both static [19] and dynamic [20] environments.

A. Related Works

The effect of the presence of people on the received RF signals is a well-known topic [21], [22] and finds its roots in the research activities about the electromagnetic (EM) propagation phenomena caused by natural or artificial obstacles during the first experimental trials at the dawn of the radio era [23]. These studies have received a great impulse after the middle of the last century, mostly for outdoor coverage applications [24]–[27]. However, despite some recent attempts to model the body-induced fading effects on short-range radio propagation [28], these research activities are mostly related to inter- [29], [30] and intrabody [31], [32] short-range radio communications. The aim of these research activities is to quantify the radio propagation losses in narrow [33] or wideband [34] indoor scenarios with the main purpose of mitigating these effects. Only a few research works [29], [35], [36] focus their attention on the geometrical relations

Manuscript received April 28, 2020; revised May 31, 2021; accepted August 19, 2021. Date of publication September 15, 2021; date of current version February 3, 2022. This work was supported by CHIST-ERA RadioSense, grant: CHIST-ERA-17-BDSI-005. This article was partially presented at the IEEE Topical Conference on Antennas and Propagation in Wireless Communications (APWC), Granada, Spain 2019. (Corresponding author: Vittorio Rampa.)

Vittorio Rampa and Stefano Savazzi are with the Institute of Electronics, Computer and Telecommunication Engineering (IEIIT), National Research Council of Italy (CNR), 20133 Milan, Italy (e-mail: vittorio.rampa@ieiit.cnr.it; stefano.savazzi@ieiit.cnr.it).

Gian Guido Gentili and Michele D'Amico are with the Dipartimento di Elettronica, Informazione e Bioingegneria (DEIB), Politecnico di Milan, 20133 Milan, Italy (e-mail: gianguido.gentili@polimi.it; michele.damico@polimi.it).

Color versions of one or more figures in this article are available at <https://doi.org/10.1109/TAP.2021.3111405>.

Digital Object Identifier 10.1109/TAP.2021.3111405

between the transmitter (TX) and the receiver (RX) location, the position and composition of the body, and its size.

A general EM model for the prediction of the mathematical relations between location, size, and composition of a *single target* and the corresponding EM field perturbation is still disputable as shown in [37] and [38] or too complex to be of practical use as based on ray-tracing techniques [30], [39] or uniform theory of diffraction (UTD) [29], [36]. Other EM methods [40]–[42], statistical [43], [44], and physical–statistical models [39], [45]–[47] are simpler than the previous ones but still limited to a single target. To the authors’ knowledge and according to the current literature, an analytical, or semianalytical, approach toward a *true multibody* model has never been tackled before. Usually, multitarget (i.e., multibody) problems have been solved by assuming the linear superposition of the single-body extra attenuations [7], [18]. However, the mutual effects induced by multiple bodies moving concurrently in the same space must be accounted for.

In [8], [10], DFL systems have been proposed to track two targets moving concurrently by using an EM model that is fully described in [48]. On the contrary, in this article, the model is generalized to an *arbitrary number of targets*. A practically usable physical–statistical model is thus designed for the prediction and the evaluation of the body-induced propagation losses, namely the RSS field, found in true N -targets scenarios with $N \geq 1$. This N -body model is able to describe both dominant static component and stochastic fluctuations of the power loss as a function of the locations of the N targets, their size, orientation, and random movements with respect to the link path.

B. Original Contributions

This article proposes an EM framework where the field perturbations induced by an arbitrary number of human bodies are modeled as a superposition of *diffraction* and *multipath* terms. The diffraction component is defined according to the scalar diffraction theory and it is characterized by the geometrical description (i.e., location, size, and orientation) and the movement characteristics (i.e., rotations and random movements around the nominal position) of N targets according to the knife-edge hypothesis [25], [49]–[51]. The multipath fading term is assumed to impair the radio link due to the presence of the bodies placed inside the sensitivity area [52] around the line-of-sight (LOS) path that connects the transmitter and the receiver. However, unlike [52], where RSS perturbations are predicted for a *single small* target [26], [52], [53] moving only in the central part of the LOS path according to the paraxial approximation [52], this novel model provides a representation of the power losses induced by *multiple* bodies having *any* size and placed *anywhere* in the area surrounding the radio link. The model presented here extends the dual-body case exploited in [8] and then presented in [48], by considering a generic EM scenario with an arbitrary number of human bodies in the surroundings of a radio link. In the former reference [8], the dual-body model is neither derived nor justified, but it is just introduced to perform DFL tasks and compare the results against other methods. In the latter reference [48], the dual-body model is derived

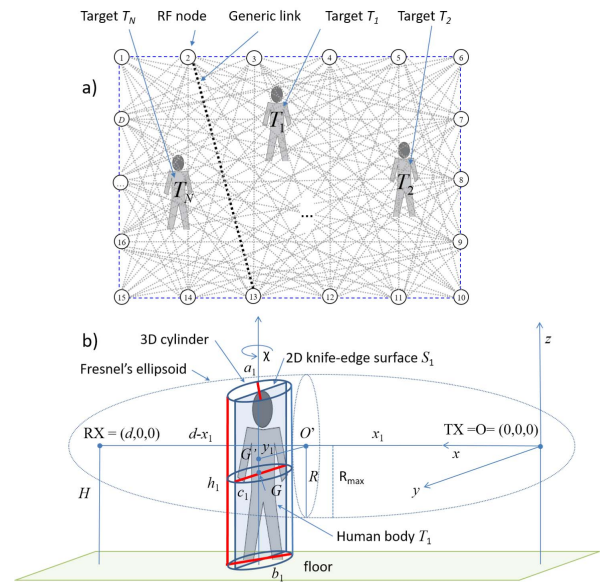


Fig. 1. (a) Generic layout of an HPS-based wireless network composed by D nodes and L links where T_n is the n th target located inside the monitored area. (b) Simplified representation of the single-link single-body scenario where the human body T_1 is sketched as a 3-D cylinder and then simplified as a 2-D knife-edge surface S_1 .

from prime principles and then described and discussed in detail. The experimental results presented here confirm that the proposed model can effectively describe the mathematical relations between the target positions and the measured RSS values. Comparisons with the results obtained with the EM simulator Feko also support the validity of the proposed model.

The novel contributions of this article are: 1) the definition of a general EM framework for the multibody scenario; 2) the derivation, from prime principles, of the full equations for the prediction of the global extra attenuation due to N bodies, or objects, in the LOS area; 3) the derivation of the analytical formulas in the case of paraxial hypothesis for the general N bodies scenario; 4) the evaluation of the extra attenuation predictions for the dual-body scenario (i.e., $N = 2$) and their comparison against the results obtained using full EM simulations; and 5) tuning of the dual-body model parameters based on field RSS measurements and comparisons of the model predictions against the aforementioned RSS measurements.

This article is organized as follows. The diffraction model that accounts for the deterministic term of the multibody induced extra attenuation is shown in Section II for any number N of the targets. The complete physical–statistical model for the prediction of the RSS field is illustrated in Section III. In particular, the dual-body model is highlighted as a practical case study. Section IV deals with the evaluation of the proposed multitarget model featuring a comparative analysis against experimental measurements and simulation results. The concluding remarks are drawn in Section V.

II. DIFFRACTION FRAMEWORK FOR THE MULTIBODY SCENARIO

As sketched in Fig. 1(a), a generic HPS consists of a mesh of partially, or completely connected, wireless network

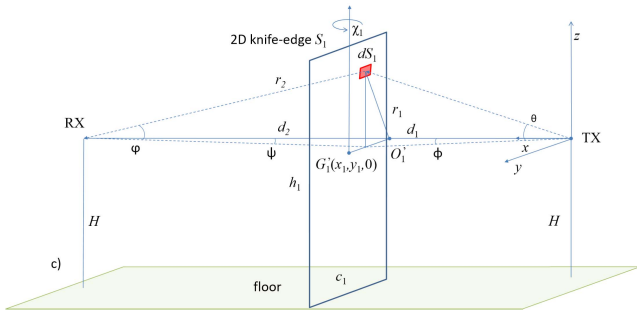


Fig. 2. Geometrical representation of the same scenario shown in Fig. 1(b), where an horizontal link of length d is positioned at distance H from the floor and a 2-D knife-edge surface S_1 , with variable transversal size c_1 and height h_1 represents the body T_1 that is placed on the floor.

composed of D RF nodes [5], [6] and $L \leq D(D-1)/2$ bidirectional links. The HPS-enabled network is composed by RF nodes that are able to perform power measurements on the RF signal and, after some processing steps, to extract body occupancy-related information. We assume that all RF nodes can measure the RSS field values at discrete time instants. No specific additional RF hardware [6] is required since RSS values are computed in the normal operations of the networked RF nodes for channel estimation/equalization and frequency/frame synchronization tasks.

Without any loss of generality, in what follows, we will focus on the single-link scenario (i.e., $L = 1$ and $D = 2$) of Fig. 1(b), by introducing the single target (T_1 being $N = 1$) first and then the multitarget (T_1, \dots, T_N with $N > 1$) cases. However, the multibody model (MBM) presented here can be exploited in a general multilink scenario with D nodes, L links, and N targets by using electric field superposition. In addition, it can be extended to make use of other physical layer channel information measures, e.g., the channel state information (CSI) and the channel quality information (CQI) [6] as well. However, this discussion is outside the scope of this work.

It is worth noticing that all the proposed models apply to a generic link of the radio network; therefore, they could be easily tailored to predict RSS over arbitrarily complex network structures for more robust body positioning, as proposed in almost all DFL methods such as [6], [7], [18]. In addition, modeling of RSS is instrumental for link selection operations, namely to identify an optimized subset of links that are most influenced by the target presence [8], [10].

A. Single-Body Model (SBM)

The single-body model (SBM) [46] is briefly recalled in this section since it is the starting point for the MBM that will be described in Section II-C. As outlined in Fig. 2, a human body (i.e., the only target T_1 located near the single-link area) is represented by a perfectly EM absorbing 3-D homogeneous cylinder with an elliptical base of minor and major axes a_1 and b_1 , respectively, that simulate the human head, torso, legs, and arms (placed near the torso). Most references assume a 3-D cylinder with a circular base [36], [54] or a 3-D prism [30], while only a few ones [35], [55] assume also that the

arms can freely move with respect to the torso. Considering a dynamic scenario where the 3-D cylinder, modeling the body, can freely move horizontally and rotate around its generic *nominal* position (x, y, z) showing different views, the target is reduced [46] to a 2-D rectangular blade (i.e., a knife-edge surface) [50], orthogonal to the LOS path at distances d_1 and d_2 from the TX and RX, respectively. The knife-edge surface is vertically placed close to the link area and can freely rotate and move showing different body views during its movements. The presence of the floor does not imply any influence on the EM propagation and it is used here only for geometrical reasons, i.e., to define the height of the link and the placement constraints of the knife-edge surface representing the body. Notice that the knife-edge approximation ignores important EM parameters, such as polarization, permittivity, conductivity, shape, radius of curvature, and surface roughness [56].

According to Fig. 1(b), the radio link is horizontally placed at distance H from the floor and the 3-D target T_1 , that is placed on the floor, is free to move and rotate around the vertical axis in the surroundings of the LOS path. The corresponding first Fresnel's zone ellipsoid [50], with radius $R = \sqrt{\lambda d_1 d_2 / d}$, does not have any contact with all other parts of the scenario (e.g., walls, ceiling, furniture, or other obstacles) except for the aforementioned target. Being $R \leq R_{\max} = \sqrt{\lambda d} / 2$, where R_{\max} is the maximum value of the radius R , λ is the wavelength, and d is the RX-TX distance (i.e., the link path length), this constraint becomes $2H > \sqrt{\lambda d}$. Notice that, as stated by standardized short-range indoor propagation models [57], ground attenuation effects may be safely ignored for a radio link inside a single indoor large room/space, e.g., a hall.

The equivalent 2-D knife-edge surface S_1 has height h_1 and width c_1 , and it is placed orthogonal to the LOS path at location $\mathbf{X}_1 = [x_1, y_1]^T$. \mathbf{X}_1 coincides with the first two coordinates of the barycenter $G_1 = (x_1, y_1, z_1)$ of the knife edge S_1 since z_1 assumes the constant value $z_1 = h_1/2 - H$. The point G'_1 is the intersection of the vertical axis passing through G_1 and the horizontal plane $z = 0$. In Sections III and IV, the position of the target T_1 (i.e., the position of G'_1) is thus identified by the off-axis displacement y_1 and the distance $x_1 = d_1$ of S_1 from the TX. However, a true person can also turn and make involuntary/voluntary movements while standing on the floor. Therefore, the 3-D target T_1 , represented by the 2-D knife-edge surface S_1 , can assume any orientation $\chi_1 \in [-\pi, \pi]$ with respect to the LOS path. It can make also some small movements $\Delta \mathbf{X}_1 = [\Delta x_1, \Delta y_1]^T$ around the nominal location \mathbf{X}_1 , thus showing a changing transversal size $c_1 = c_1(a_1, b_1, \chi_1)$, with $a_1 \leq c_1 \leq b_1$, and a varying location $\mathbf{X}_1 + \Delta \mathbf{X}_1$.

According to the scalar theory of diffraction, the electric field at the RX, which is generated by the isotropic source in TX, is modified by the presence of the 2-D knife-edge surface S_1 located in the link area [46]. It can be predicted [26] as being generated by a virtual array of Huygens' sources located on S_1 but not belonging to the obstacle itself. In far-field propagation conditions, the electric field dE at the RX, due to the diffraction effects caused by the elementary Huygens'

source of area dS_1 with coordinates (x, y, z) , is given by

$$dE = j \frac{E_0 d}{\lambda r_1 r_2} \exp\left\{-j \frac{2\pi}{\lambda}(r_1 + r_2 - d)\right\} dS_1 \quad (1)$$

where r_1 and r_2 are the distances of the generic elementary area dS_1 for the TX and RX, respectively. E_0 is the free-space electric field that is described by the following equation:

$$E_0 = -j \frac{\eta I \ell}{2 \lambda d} \exp\left(-j \frac{2\pi d}{\lambda}\right) \quad (2)$$

with η being the free-space impedance and $I \ell$ the momentum of the source. The electric field at the RX is given by [46]

$$E = -j \frac{\eta I \ell}{2 \lambda d} \exp\left(-j \frac{2\pi d}{\lambda}\right) \cdot \left\{1 - j \frac{d}{\lambda} \int_{S_1} \frac{1}{r_1 r_2} \exp\left\{-j \frac{2\pi}{\lambda}(r_1 + r_2 - d)\right\} dS_1\right\} \quad (3)$$

where the first term refers to the electric field (2) due to the free-space propagation in the empty scenario and the second term includes the diffraction effects due to the body presence according to (1). The integral of the second term is computed over the rectangular domain defined by the S_1 region defined as $S_1 = \{(x, y, z) \in \mathbb{R}^3 : x = x_1 = d_1, \text{ and } y_1 - c_1/2 \leq y \leq y_1 + c_1/2, -H \leq z \leq h_1 - H\}$. Focusing on the *extra attenuation* induced by the body with respect to the free space, (3) can be written as

$$\frac{E}{E_0} = 1 - j \frac{d}{\lambda} \int_{S_1} \frac{1}{r_1 r_2} \exp\left\{-j \frac{2\pi}{\lambda}(r_1 + r_2 - d)\right\} dS_1. \quad (4)$$

In fact, according to (4), the presence of the body induces an extra attenuation $A_{dB} = -10 \log_{10} |E/E_0|^2$ with respect to the free-space propagation. Being a forward-only method, the diffraction model holds only for the generic target T_1 placed in the area \mathcal{Y} near the radio link where it is $\mathcal{Y} = \{(x, y) \in \mathbb{R}^2 : 0 < x < d; -\infty < y < +\infty\}$. Of course, as shown in [46], the effect of the target presence vanishes for large but finite values of $|y|$.

B. Paraxial Single-Body Model (PSBM)

By exploiting the paraxial approximation and the variable substitutions $u = y(\sqrt{2}/R_1)$ and $v = z(\sqrt{2}/R_1)$, (4) reduces to the paraxial single-body model (PSBM) equation defined as

$$\frac{E}{E_0} = 1 - \frac{1}{2} j \int_{(\sqrt{2}y_1 - c_1/\sqrt{2})/R_1}^{(\sqrt{2}y_1 + c_1/\sqrt{2})/R_1} \exp\left(-j \frac{\pi}{2} u^2\right) du \cdot \int_{-\sqrt{2}H/R_1}^{+\sqrt{2}(h_1 - H)/R_1} \exp\left(-j \frac{\pi}{2} v^2\right) dv \quad (5)$$

where Fresnel's radius $R_1 = R(x_1)$ is given by $R_1 = \sqrt{\lambda x_1 (d - x_1)/d}$. Here, we have specified that the generic Fresnel's radius R of Fig. 1(b) is equal to $R(x_1)$ to explicitly highlight that it is related to the position x_1 of target T_1 . Equation (5) can be easily computed by using Fresnel's sine and cosine integrals [52]. The paraxial approximation implies the following assumptions: $\max\{|y_1|, |z_1|, h_1, c_1, \lambda\} \ll \min\{x_1, d - x_1\}$, $\cos \varphi \simeq 1$, $\cos \theta \simeq 1$, $\cos \psi \simeq 1$, and $\cos \phi \simeq 1$, where the aforementioned angles are shown in

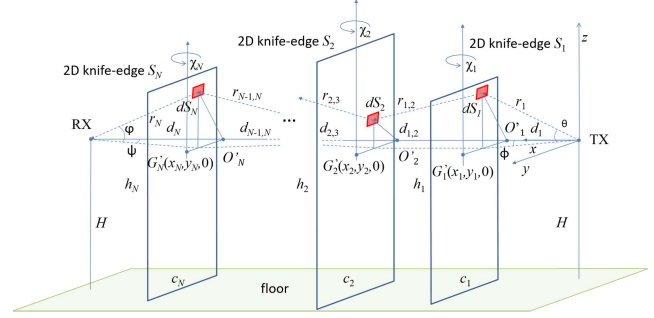


Fig. 3. Single-link multitarget ($N > 1$) scenario composed by an horizontal single-link of length d , placed at distance H from the floor, and N different 2-D equivalent knife-edge surfaces S_1, S_2, \dots, S_N corresponding to the targets T_1, T_2, \dots, T_N located in $\mathbf{X}_1, \mathbf{X}_2, \dots, \mathbf{X}_N$, respectively.

Fig. 2. The model gives valid predictions in the same area \mathcal{Y} defined for the SBM model. The paraxial approximation is mainly used for outdoor scenarios, namely for terrestrial radio propagation applications [24], [25] where it holds gracefully. However, it has also been employed in HPS applications [58], even if this paraxial hypothesis limits the validity of (5) to small bodies near the central area of the radio link. For more details about single-target modeling derived from (4), e.g., for models that include vertical or horizontally polarization, the interested reader can refer to [46].

C. Multibody Model (MBM)

According to Fig. 3, the multibody scenario is a generalization of the single-target case shown in Fig. 2. N knife-edge surfaces stand vertically on the floor and are placed orthogonally to the LOS path. They are numbered from 1 up to N according to their increasing distances from the TX. Knife-edge positions are identified by the column vectors $\mathbf{X}_n = [x_n, y_n]^T$ that correspond to the projections $G'_n = (x_n, y_n, 0)$ of knife-edge barycenters $G_n = (x_n, y_n, z_n)$ with $z_n = h_n/2 - H$. The positions of all targets are thus identified by the column vector $\mathbf{X} = [\mathbf{X}_1^T, \mathbf{X}_2^T, \dots, \mathbf{X}_N^T]^T$. The single n th target T_n , with $1 \leq n \leq N$, is described by the rotating knife-edge surface S_n having height h_n , traversal size $c_n = c_n(a_n, b_n, \chi_n)$ with constraint $a_n \leq c_n \leq b_n$, and orientation $\chi_n \in [-\pi, \pi]$ with respect to the LOS path, with obvious meaning of these terms already mentioned in Section II-A. All geometrical and motion parameters are organized in the following column vectors: $\mathbf{c} = [c_1, c_2, \dots, c_N]^T$ collecting the knife-edge traversal sizes, $\mathbf{h} = [h_1, h_2, \dots, h_N]^T$ and $\boldsymbol{\chi} = [\chi_1, \chi_2, \dots, \chi_N]^T$, collecting both target heights and the orientations, as well. It is also $\mathbf{a} = [a_1, a_2, \dots, a_N]^T$ and $\mathbf{b} = [b_1, b_2, \dots, b_N]^T$. Finally, $\forall \Delta x_n, \Delta y_n \in [-B + B]$, the column vector $\Delta \mathbf{X} = [\Delta \mathbf{X}_1^T, \Delta \mathbf{X}_2^T, \dots, \Delta \mathbf{X}_N^T]^T$ tracks the involuntary/voluntary movements of the bodies in the position interval $[-B + B]$ (supposed symmetrically arranged) around the nominal position vector \mathbf{X} .

For $N > 1$ targets, the knife-edge diffraction model (1) still holds true for each n th surface S_n , although (4) is no longer valid. The LOS path is now divided into $N + 1$ segments of length equal to $d_1, d_{1,2}, d_{2,3}, \dots, d_{N-1,N}, d_N$ with $d = d_1 + \sum_{n=1}^{N-1} d_{n,n+1} + d_N$. Generalizing the model of Section II-A for N targets, the term $r_{n,n+1}$ represents the distance between

two consecutive elementary areas dS_n and dS_{n+1} , while the terms r_1 and r_N represent the distance between the transmitter and dS_1 and the distance between dS_N and the receiver, respectively. The n th elementary area $dS_n = d\zeta_n d\varsigma_n$ is located on the n th plane S_n that is identified by its position \mathbf{X}_n . The coordinate axes ζ_n and ς_n (for clarity not shown in Fig. 3) have the origin in O'_n and directed as the y and z axes. As an additional hypothesis with respect to the ones of Section II-A, only forward propagation from TX to RX is considered with no backward-scattered waves between any surfaces S_n and the RX (i.e., both single- and multiple-scattering effects between knife edges are ignored).

In far-field conditions, by assuming only forward propagation, $\forall T_n$ with $n = 1, \dots, N-1$, the elementary electric field dE_{n+1} due to the diffraction effects caused by the elementary Huygens' source of area dS_n is computed at dS_{n+1} by considering the distance $r_{n,n+1}$ between the elements dS_n and dS_{n+1} according to

$$dE_{n+1} = j \frac{dE_n dS_n}{\lambda r_{n,n+1}} \exp\left(-j \frac{2\pi r_{n,n+1}}{\lambda}\right). \quad (6)$$

The electric field E_1 , impinging on the first target, is

$$E_1 = E_0 \left(\frac{d}{r_1}\right) \exp\left(-j \frac{2\pi(r_1 - d)}{\lambda}\right) \quad (7)$$

while the electric field dE that is measured at the RX node and generated by the area dS_N of the target N closest to the RX is given by

$$dE = j \frac{dE_N dS_N}{\lambda r_N} \exp\left(-j \frac{2\pi r_N}{\lambda}\right). \quad (8)$$

Combining (6)–(8), it is

$$\begin{aligned} dE = & j^N \frac{d}{\lambda^N r_N r_{N-1,N}, \dots, r_{1,2} r_1} E_0 \\ & \cdot \exp\left\{-j \frac{2\pi}{\lambda}(r_N + r_{N-1,N} + \dots + r_{1,2} + r_1 - d)\right\} \\ & \cdot dS_1 dS_2, \dots, dS_N. \end{aligned} \quad (9)$$

To obtain the electric field E , (9) must be integrated over the domain $S^{(c)} = \bigcup_{n=1}^N S_n^{(c)}$ where each region $S_n^{(c)}$ corresponds to the 2-D plane $\mathcal{P}_n \supset S_n$ that does not contain the points of the knife-edge surface S_n . Equation (9) now becomes

$$\begin{aligned} \frac{E}{E_0} = & j^N \int_{S_1^{(c)}} \int_{S_2^{(c)}} \dots \int_{S_N^{(c)}} \frac{d}{\lambda^N r_N r_{N-1,N}, \dots, r_{1,2} r_1} \\ & \cdot \exp\left\{-j \frac{2\pi}{\lambda}(r_N + r_{N-1,N} + \dots + r_{1,2} + r_1 - d)\right\} \\ & \cdot dS_1 dS_2, \dots, dS_N. \end{aligned} \quad (10)$$

We now define $E^{(n)}$ as the value of the electric field at the RX node when only one target, i.e., the n -th body or obstacle, is present in the LOS area. Similarly, $E^{(n,m)}$ refers to the electric field at the receiver when only two targets, i.e., the n th and m -th obstacles out of N , are in the link area and so on. The notation $E^{(1,2,\dots,N)}$ thus highlights the contributions of the N targets to the link loss: this is the total electric field E at the receiver given by (10). Considering the above definitions, (10) may be rewritten to highlight the mutual interactions of the

targets, grouped by $\binom{N}{N-1}$ singles, $\binom{N}{N-2}$ pairs, $\binom{N}{N-3}$ triples, and so on as

$$\begin{aligned} (-1)^N \frac{E^{(1,2,\dots,N)}}{E_0} = & -1 + \underbrace{\sum_{n=1}^N \frac{E^{(n)}}{E_0}}_{\text{singles}} - \underbrace{\sum_{n=1}^{N-1} \sum_{m=n+1}^N \frac{E^{(n,m)}}{E_0}}_{\text{pairs}} \\ & + \underbrace{\sum_{n=1}^{N-2} \sum_{m=n+1}^{N-1} \sum_{k=m+1}^N \frac{E^{(n,m,k)}}{E_0}}_{\text{triples}} + \dots \\ & + \Psi(S_1, \dots, S_N) \end{aligned} \quad (11)$$

where the last term $\Psi(S_1, \dots, S_N)$

$$\begin{aligned} \Psi(S_1, \dots, S_N) = & j^N \int_{S_1} \int_{S_2}, \dots, \int_{S_N} \frac{d}{\lambda^N r_N r_{N-1,N}, \dots, r_{1,2} r_1} \\ & \cdot \exp\left\{-j \frac{2\pi}{\lambda}(r_N + r_{N-1,N} + \dots \right. \\ & \left. \dots + r_{1,2} + r_1 - d)\right\} \cdot dS_1 dS_2, \dots, dS_N \end{aligned} \quad (12)$$

is the integral computed over the composite domain defined by the union $S^{(1,2,\dots,N)} = \bigcup_{n=1}^N S_n$ of the N rectangular knife-edge surfaces S_n . The knife-edge surfaces (Fig. 3) have the following definitions: for $n = 1$, it is $S_1 = \{(x, y, z) \in \mathbb{R}^3 : x = x_1 = d_1, y_1 - c_1/2 \leq y \leq y_1 + c_1/2, -H \leq z \leq h_1 - H\}$, while $\forall n = 2, \dots, N$, it is also $S_n = \{(x, y, z) \in \mathbb{R}^3 : x = x_n = d_1 + \sum_{i=1}^{n-1} d_{i,i+1}, \text{ and } y_n - c_n/2 \leq y \leq y_n + c_n/2, -H \leq z \leq h_n - H\}$.

Using (11), for a generic number of targets N , the electric field ratio $(E^{(1,2,\dots,N)})/E_0$ due to N obstructing bodies is composed by the single-target contributions $(E^{(n)})/E_0$, for $n = 1, \dots, N$ terms, the target pairs, $(E^{(n,m)})/E_0$, for $n = 1, \dots, N-1, m = n+1, \dots, N$, the triples, $(E^{(n,m,k)})/E_0$, for $n = 1, \dots, N-2, m = n+1, \dots, N-1, k = m+1, \dots, N$, and so on, up to the contributions of the $N-1$ target group. Likewise PSBM and SBM, MBM gives valid predictions when the targets are placed in the area \mathcal{Y} near the LOS path, as defined in Section II-A.

When two bodies are in the area \mathcal{Y} , the received electric field $E^{(1,2)}$ embeds the mutual effects of the two targets T_1 (i.e., S_1) and T_2 (i.e., S_2) on the radio propagation. $E^{(1,2)}$ is computed from the single-target terms $E^{(1)}$ and $E^{(2)}$ as

$$\frac{E^{(1,2)}}{E_0} = -1 + \frac{E^{(1)}}{E_0} + \frac{E^{(2)}}{E_0} + \Psi(S_1, S_2) \quad (13)$$

where the *mixed* term that depends on both knife edges S_1 and S_2 is defined according to (12) as

$$\begin{aligned} \Psi(S_1, S_2) = & - \int_{S_1} \int_{S_2} \frac{d}{\lambda^2 r_2 r_{1,2} r_1} \\ & \cdot \exp\left\{-j \frac{2\pi}{\lambda}(r_2 + r_{1,2} + r_1 - d)\right\} dS_1 dS_2. \end{aligned} \quad (14)$$

In particular, from (13), the term $E^{(1)}$ quantifies the effect of the target T_1 alone in the link area according to (4). It depends on the corresponding target size c_1 , the target height h_1 , the link height H from the floor, and the distances d_1 and $d - d_1 = d_2 + d_{12}$ of the body T_1 from the TX and RX, respectively.

Likewise, $E^{(2)}$ refers to the contributions of target T_2 only, according to its target size c_2 and height h_2 , the link height H from the floor, and the distances $d_1 + d_{12}$ and d_2 of the body T_2 from the TX and RX, respectively.

For $N = 1$, the proposed MBM reduces to the single-body model (SBM) as expected since all singles, pairs, triples, and other high-order terms of (11) vanish except for the term $\Psi(S_1)$. The MBM model for $N = 2$ targets (13) has been initially introduced in [48] along with some preliminary results. Further results obtained in DFL scenarios have been presented in [10] as well. This dual-target model can be directly obtained from (10) or, equivalently, (11). Model comparisons are presented in Section IV.

D. Paraxial Multibody Model (PMBM)

For HPS applications, paraxial hypotheses are realistic only for small target(s), namely for small enough c_i and h_i with respect to the path length d . The approximation also requires the subject to move nearby the LOS path, with small enough y_i and z_i , or located in the central part of the LOS path. Carrier wavelength λ is also much smaller than the distances x_i and $d - x_i$ (Section II-B). However, since the paraxial approximation is useful in several applications, mostly outdoor, in this section, we will approximate the full (10) or (11) using paraxial assumptions, namely the paraxial MBM (PMBM) model.

Based on the paraxial approximation, (10) becomes

$$\begin{aligned} \frac{E}{E_0} &= \left(\frac{j}{2}\right)^N \int_{S_1^{(c)}} \int_{S_2^{(c)}} \cdots \int_{S_N^{(c)}} \\ &\times \frac{d d_{1,2} d_{2,3}, \dots, d_{N-1,N}}{(d_1 + d_{1,2})(d_{1,2} + d_{2,3}), \dots, (d_{N-1,N} + d_N)} \\ &\cdot \exp\left\{-j\frac{\pi}{2}(u_1^2 + u_2^2 + \cdots + u_N^2 - 2\alpha_{1,2}u_1u_2 \cdots \right. \\ &\quad \left. + - 2\alpha_{N-1,N}u_{N-1}u_N)\right\} du_1 du_2, \dots, du_N \\ &\cdot \exp\left\{-j\frac{\pi}{2}(v_1^2 + v_2^2 + \cdots + v_N^2 - 2\alpha_{1,2}v_1v_2 \cdots \right. \\ &\quad \left. + - 2\alpha_{N-1,N}v_{N-1}v_N)\right\} dv_1 dv_2, \dots, dv_N. \end{aligned} \quad (15)$$

In the Appendix, we show how to rewrite (15) to reveal the mutual interactions of targets as in (11).

For the case of $N = 2$ targets, (15) becomes now analytically tractable. Using the formulation shown in (13), adapted in the Appendix for paraxial assumptions, it is

$$\begin{aligned} \frac{E^{(1,2)}}{E_0} &= -1 + \frac{E^{(1)}}{E_0} + \frac{E^{(2)}}{E_0} - \frac{1}{4} \frac{d d_{1,2}}{(d_1 + d_{1,2})(d_{1,2} + d_2)} \\ &\cdot \int_{-\sqrt{2}H/R_1}^{+\sqrt{2}(h_1-H)/R_1} \int_{-\sqrt{2}H/R_2}^{+\sqrt{2}(h_2-H)/R_2} \\ &\times \exp\left\{-j\frac{\pi}{2}(u_1^2 + u_2^2 - 2\alpha_{1,2}u_1u_2)\right\} du_1 du_2 \\ &\cdot \int_{(\sqrt{2}y_1+c_1/\sqrt{2})/R_1}^{(\sqrt{2}y_1+c_1/\sqrt{2})/R_1} \int_{(\sqrt{2}y_2+c_2/\sqrt{2})/R_2}^{(\sqrt{2}y_2+c_2/\sqrt{2})/R_2} \\ &\cdot \int_{(\sqrt{2}y_1-c_1/\sqrt{2})/R_1}^{(\sqrt{2}y_1-c_1/\sqrt{2})/R_1} \int_{(\sqrt{2}y_2-c_2/\sqrt{2})/R_2}^{(\sqrt{2}y_2-c_2/\sqrt{2})/R_2} \\ &\times \exp\left\{-j\frac{\pi}{2}(v_1^2 + v_2^2 - 2\alpha_{1,2}v_1v_2)\right\} dv_1 dv_2 \end{aligned} \quad (16)$$

where u_1, u_2, v_1, v_2 , the constant terms R_1, R_2 , and $\alpha_{1,2}$ are defined in the cited Appendix. Notice that, some approximated models are already available in the literature [25], [49] for the evaluation of the extra attenuation due to multiple semi-infinite knife-edge surfaces. These models can be obtained by using the paraxial approximation over the semi-infinite domains representing the targets (unlike the *finite* target size assumption adopted here). They are typically effective in outdoor scenarios for the prediction of propagation loss over nonregular terrain profiles. The interested reader can refer to [27] and references therein for a brief discussion and model comparisons.

E. Additive Models

Based on the analysis of Sections II-B–II-D, the term $|E^{(1,2,\dots,N)}/E_0|$ for N targets can be used to evaluate the extra attenuation $A_{\text{dB}}^{(1,2,\dots,N)}$ with respect to the free-space (i.e., unobstructed or empty) scenario as

$$A_{\text{dB}}^{(1,2,\dots,N)} = -10 \log_{10} |E^{(1,2,\dots,N)}/E_0|^2. \quad (17)$$

From (11), it is apparent that the extra attenuation terms $|(E^{(1)}/E_0)|, |(E^{(2)}/E_0)|, \dots, |(E^{(N)}/E_0)|$ alone or, equivalently, $A_{\text{dB}}^{(1)}, A_{\text{dB}}^{(2)}, \dots, A_{\text{dB}}^{(N)}$, are not sufficient to evaluate $|E^{(1,2,\dots,N)}/E_0|$ since: 1) the phase relations between the terms $(E^{(m)}/E_0)$ are unknown; 2) the terms $(E^{(n,m)}/E_0), (E^{(n,m,k)}/E_0), \dots$, are not available; and 3) the interaction terms between the targets that are expressed by the integral of the right-hand side of (11) are not known as well. These facts limit the use of single-target measurements for the multiple-target case. According to these considerations, the additive hypothesis, namely $A_{\text{dB}}^{(1,2,\dots,N)} = A_{\text{dB}}^{(1)} + A_{\text{dB}}^{(2)} + \cdots + A_{\text{dB}}^{(N)}$, which is generally exploited in various forms in the literature [7], [18], is a rather superficial approximation. For the case of two targets ($N = 2$), in Section IV-C, an additive SBM model is proposed where the individual extra attenuations $A_{\text{dB}}^{(1)}, A_{\text{dB}}^{(2)}, \dots, A_{\text{dB}}^{(N)}$, follow the SBM model described in (4). Limitations of such representation are highlighted by a comparison with the MBM and PMBM models. Similar considerations apply also to the additive PSBM model.

F. Analysis of Model Limitations and Suitable Scenarios

The body models previously discussed have some limitations due to the assumptions adopted for their derivation. For the sake of convenience and to highlight the most suitable scenarios where such models can be effectively applied, these limitations are reviewed in the following.

General limitations common to all the defined models of Section II-A up to Section II-D are listed in the following.

- 1) The scalar theory of diffraction does not include any polarization effect.
- 2) Far-field propagation is assumed, i.e., $d_1, d_2, \dots, d_N \gg \lambda$: this implies that, when bodies are too close to the RF nodes, the predicted values may have large errors. Given the wavelength ($\simeq 12$ cm), this is usually not an issue.
- 3) All models represent true bodies as homogeneous and perfectly absorbing 3-D cylinders [46] without including any permittivity, conductivity [36], [54], shape, radius of curvature, and surface roughness [56] effects.

- 4) These 3-D cylinders are furthermore simplified by reducing them to 2-D knife-edge surfaces [26]: the dimensions of the knife edges are model parameters that have to be estimated (see Section IV-B).
- 5) All models hold only for generic body(ies) T_i placed in the area \mathcal{Y} near the radio link where it is $\mathcal{Y} = \{(x, y) \in \mathbb{R}^2 : 0 < x < d; -\infty < y < +\infty\}$.

Model-specific limitations should also be considered for each identified model.

- 1) PSBM and PMBM exploit the paraxial approximation (Section II-B) and are useful for outdoor scenarios with long links [24], [25], where the target(s) (mostly buildings or other artificial obstacles) are smaller w.r.t. the link length d .
- 2) SBM and MBM do not exploit any paraxial approximations and can be applied to both indoor and outdoor scenarios depending on the number of bodies that are present in the link area.
- 3) MBM and PMBM assume only forward propagation from the TX to the RX and ignores single and multiple reverberations among bodies nearby: this means that they may underestimate the number of body present in crowded configurations, if too close to each other.
- 4) Additive SBM and PSBM compute the multibody extra attenuation (in dB) by summing single-body attenuations (in dB), but this is a very coarse approximation as already shown in Section II-E.

Notice that, for all models, multipath effects due to log-normal impairments [59] are ignored as introduced later on in Section III. Within the considered hypotheses framework, the MBM (for the multibody scenario) and the SBM (for the single-body scenario) models can be considered, for their simplicity, as the reference models for HPS systems.

III. PHYSICAL-STATISTICAL MULTIBODY MODEL

In this section, we propose a true multitarget physical-statistical model that relates the RSS to the link geometry (d , H), the bodies locations \mathbf{X} , and their geometrical sizes (i.e., \mathbf{c} and \mathbf{h}). In addition to the diffraction, or physical, component analyzed in Section II, the additional statistical component quantifies the uncertainty of body movements, modeled here by small random voluntary/involuntary motions $\Delta\mathbf{X}$ and rotations $\boldsymbol{\chi}$ around the nominal position \mathbf{X} , as well as multipath fading, multiple scattering between bodies, backward propagation effects, and other random fluctuations, not included in the diffraction terms. For the sake of simplicity, in Section IV, all geometrical parameters defined in Section II-C will be represented by the compact set $\boldsymbol{\Lambda} = \{\mathbf{a}, \mathbf{b}, \mathbf{h}, d, H\}$.

Let P be the RSS measurement performed by the RX and expressed in dBm, and the power measurement P can be modeled as the sum of: 1) the deterministic term $P_0 = \text{EIRP} - A_{\text{dB}}^0 + G_R$ due to the free-space propagation, being EIRP the equivalent isotropically radiated power (in dBm), $A_{\text{dB}}^0 = -20 \log_{10}(\lambda/4\pi d)$ the free-space loss (in dB), and G_R the receiver antenna gain (in dBi); 2) the extra attenuation term w.r.t. the free-space loss $A_{\text{dB}} = A_{\text{dB}}^{(1,2,\dots,N)}$ (in dB),

as in (17), caused by the body-induced diffraction terms; and 3) the Gaussian random term w (in dB) that includes the lognormal multipath effects [59], the measurement noise and the other random disturbances assumed normally distributed. Thus, it is

$$P = \begin{cases} P_0 - A_{\text{dB}}^{(1,2,\dots,N)} + w, & \text{if } f \exists \mathbf{X}_n \in \mathcal{Y} \\ P_0 + w_0, & \text{elsewhere.} \end{cases} \quad (18)$$

The free-space term P_0 depends only on the geometry of the scenario, the transmitted power, the gain and configuration of the antennas, and the propagation coefficients [53]. The term $A_{\text{dB}}^{(1,2,\dots,N)} = A_{\text{dB}}(\mathbf{X}, \Delta\mathbf{X}, \boldsymbol{\chi}, \boldsymbol{\Lambda})$, evaluated according to (17), is the extra attenuation expressed in dB due to the body-induced diffraction with respect to the free-space scenario. It is computed using (10) or (11) for MBM and (15) or (23) for PMBM. Propagation effects not included in the diffraction models (10) or (11) are modeled by the Gaussian noise $w \sim \mathcal{N}(\Delta\mu_C, \sigma_0^2 + \Delta\sigma_C^2)$ with $\Delta\mu_C$ and $\Delta\sigma_C^2$ being the residual stochastic body-induced multipath fading mean and variance terms [52], [58]. The term σ_0^2 models the power fluctuations induced by environmental changes outside the link area and not attributable to body movements around the LOS link.

For the empty scenario, where nobody is present in the link area, namely the *background* configuration, the RSS is simply modeled as $P = P_0 + w_0$ with $w_0 \sim \mathcal{N}(0, \sigma_0^2)$. Notice that in HPS systems, $\mu_0 = E_{w_0}[P] = P_0$ and $\sigma_0^2 = \text{Var}_{w_0}[P]$ can be evaluated from field measurements in the empty scenario during a calibration phase. On the contrary, the presence of people modifies both the mean $\mu_1(\mathbf{X}) = E_{\boldsymbol{\chi}, \Delta\mathbf{X}, w}[P]$ and the variance $\sigma_1^2(\mathbf{X}) = \text{Var}_{\boldsymbol{\chi}, \Delta\mathbf{X}, w}[P]$ terms. Based on (18), the mean $\mu(P)$ and variance $\sigma^2(P)$ are defined as

$$\mu(P) = \begin{cases} \mu_1(\mathbf{X}|\boldsymbol{\Lambda}) = P_0 + \Delta\mu(\mathbf{X}|\boldsymbol{\Lambda}), & \text{if } f \exists \mathbf{X}_n \in \mathcal{Y} \\ \mu_0 = P_0, & \text{elsewhere} \end{cases} \quad (19)$$

and

$$\sigma^2(P) = \begin{cases} \sigma_1^2(\mathbf{X}|\boldsymbol{\Lambda}) = \sigma_0^2 + \Delta\sigma^2(\mathbf{X}|\boldsymbol{\Lambda}), & \text{if } f \exists \mathbf{X}_n \in \mathcal{Y} \\ \sigma_0^2, & \text{elsewhere} \end{cases} \quad (20)$$

where it is emphasized the dependency of P from the position \mathbf{X}_n of at least one target T_n in the area \mathcal{Y} and the geometrical coefficients $\boldsymbol{\Lambda}$. The RSS average $\Delta\mu(\mathbf{X}) = \mu_1(\mathbf{X}) - \mu_0$ and variance $\Delta\sigma^2(\mathbf{X}) = \sigma_1^2(\mathbf{X}) - \sigma_0^2$ increments are defined as

$$\Delta\mu(\mathbf{X}|\boldsymbol{\Lambda}) = \Delta\mu_C - E_{\boldsymbol{\chi}, \Delta\mathbf{X}}[A_{\text{dB}}(\mathbf{X}|\Delta\mathbf{X}, \boldsymbol{\chi}, \boldsymbol{\Lambda})] \quad (21)$$

and

$$\Delta\sigma^2(\mathbf{X}|\boldsymbol{\Lambda}) = \Delta\sigma_C^2 + \text{Var}_{\boldsymbol{\chi}, \Delta\mathbf{X}}[A_{\text{dB}}(\mathbf{X}|\Delta\mathbf{X}, \boldsymbol{\chi}, \boldsymbol{\Lambda})]. \quad (22)$$

The term $A_{\text{dB}}(\mathbf{X}|\Delta\mathbf{X}, \boldsymbol{\chi}, \boldsymbol{\Lambda})$ highlights the fact that, given the geometrical parameters $\boldsymbol{\Lambda}$ and the motion terms $\Delta\mathbf{X}$, $\boldsymbol{\chi}$, the extra attenuation is only a function of the positions \mathbf{X} of the bodies. In the following, we assume that the bodies are positioned in \mathbf{X} , but each of them can slightly change its location and posture making small random movements $\Delta\mathbf{X}_n$ with $\Delta x_n, \Delta y_n \sim \mathcal{U}(-B, +B)$ and rotations $\chi_n \sim \mathcal{U}(-\pi, +\pi)$ around the vertical axis. $\mathcal{U}(\alpha, \beta)$ indicates the uniform distribution within the interval $[\alpha, \beta]$, while for each n , the set $[-B + B] \times [-B + B]$ defines the 2-D area around the

nominal coordinate position \mathbf{X}_n where the n th target can freely move. To determine (21) and (22), the mean $E_{\chi, \Delta \mathbf{X}}[\cdot]$ and the variance $\text{Var}_{\chi, \Delta \mathbf{X}}[\cdot]$ are computed over the aforementioned uniform distribution of $\Delta \mathbf{X}$ and χ .

The residual body-induced multipath terms $\Delta \mu_C$ and $\Delta \sigma_C^2$ in (21) and (22), respectively, can be directly evaluated from field measurements performed during the calibration phase. However, these terms are marginally influenced by the specific body locations, as also shown in [59] and [52], and are thus not relevant for HPS applications. On the contrary, the diffraction term $A_{\text{dB}}(\mathbf{X}|\Delta \mathbf{X}, \chi, \Lambda)$ provides a simple but effective method to predict the power perturbation $\Delta \mu(\mathbf{X}|\Lambda)$ and $\Delta \sigma^2(\mathbf{X}|\Lambda)$ as a function of the body position and size.

IV. MODEL OPTIMIZATION AND EVALUATION

To confirm the validity of the proposed MBMs, several EM simulations with the Feko software environment and on-field experiments have been carried out according to the same link scenario sketched in Fig. 3. Feko¹ implements time- and frequency-domain full-wave solvers, such as the method of moments (MoM), the finite difference time domain (FDTD) method, the finite element method (FEM) and the multi level fast multipole method (MLFMM). For details about the solvers, the interested reader may have a look at [60].

First of all, simulations have been carried out to compare the results of the diffraction-based MBM and PMBM models shown in Sections II-C and II-D, respectively, with the ones obtained with Feko. Next, we have compared the aforementioned models against the RSS measurements obtained from IEEE 802.15.4 devices [61], commonly used in industrial applications [62]. Considering the application to multibody localization featuring $N = 2$ targets, the MBM and PMBM model parameters, namely the geometrical sizes (i.e., \mathbf{a} , \mathbf{b} and \mathbf{h}) of the knife-edge surfaces, are optimized using a small subset of the experimental data so that they could effectively model the obstructions induced by the true targets. The proposed models using optimized sizes of the knife-edges are then validated over different configurations, where both targets move along the LOS link.

It is worth noticing that Feko simulations are related to perfect electric conductor (PEC) configurations to describe knife-edge targets. On the contrary, MBM and PMBM 2-D models assume perfectly absorbing surfaces. The MBM and PMBM models also ignore important EM parameters, e.g., polarization (see Section II-F), that, on the contrary, are considered by Feko.

A. Model Comparison Against EM Simulations

The MBM and PMBM models are evaluated and compared in this section with the results from EM simulations for a path length $d = 5.0$ m and frequency $f_c = 2.4868$ GHz. To this aim, the free-space loss A_{dB}^0 in the empty scenarios for both Feko simulations and MBM/PMBM predictions is set to $A_{\text{dB}}^0 = 54.33$ dB. To simplify the EM simulation complexity (mostly due to the long Feko runs), in what follows MBM

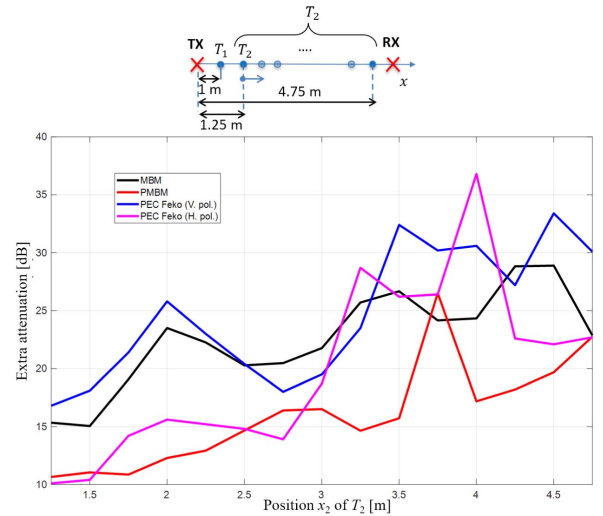


Fig. 4. Feko PEC simulations for vertically (blue line) and horizontally (magenta line) polarized source versus MBM (black line) and PMBM (red line) $A_{\text{dB}}^{(1,2)}$ predictions for targets T_1 and T_2 along the LOS path as shown in the scenario on the top.

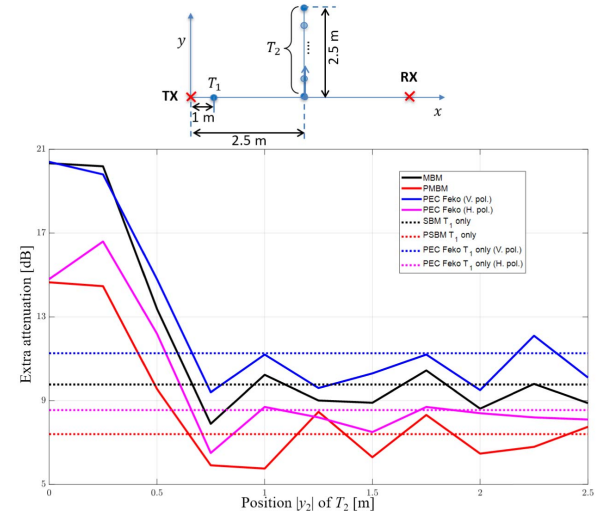


Fig. 5. Feko PEC simulations for vertically (blue line) and horizontally (magenta line) polarized source versus MBM (black line) and PMBM (red line) $A_{\text{dB}}^{(1,2)}$ predictions for the target T_1 along the LOS path and T_2 across the LOS path as shown in the scenario on the top. The dotted lines (with the same colors adopted for the dual-target cases) show the extra attenuation predicted by the previous models/simulations due to the presence of the target T_1 only.

and PMBM models are compared in a dual-target scenario ($N = 2$) only. Figs. 4 and 5 show the predicted values of the extra attenuation $A_{\text{dB}}^{(1,2)} = -10 \log_{10} |E^{(1,2)}|/E_0|^2$ computed according to the models described by (13) and (16), namely MBM and PMBM, respectively. Thus, the total path loss A_{dB} in the dual-target scenario is equal to $A_{\text{dB}} = A_{\text{dB}}^0 + A_{\text{dB}}^{(1,2)}$.

No movements/rotations are allowed and the two targets are placed in their nominal positions; in both figures, the target T_1 is fixed in the position $\mathbf{X}_1 = [1.0, 0.0]^T$, while the other target T_2 changes its positions along and across the LOS path. In Fig. 4, T_2 is placed in $\mathbf{X}_2 = [x_2, 0.0]^T$ and moves along the LOS path with $1.25 \leq x_2 \leq d - 0.25$ m and 0.25 m increments

¹The commercial EM simulator designed by Altair Engineering Inc.

TABLE I
AVERAGE ERRORS AND STANDARD DEVIATIONS OBTAINED BY MBM AND
PMBM MODELS VERSUS FEKO PEC V. POL. SIMULATIONS

Errors/St.dev.	LOS area	
	Along LOS	Across LOS
ϵ_{MBM}	-2.07 dB	-0.98 dB
σ_{MBM}	3.36 dB	0.74 dB
$\epsilon_{\text{MBM}}^{\text{R}}$	-2.44 %	-1.50 %
$\sigma_{\text{MBM}}^{\text{R}}$	4.08 %	1.11 %
ϵ_{PMBM}	-8.69 dB	-4.00 dB
σ_{PMBM}	4.37 dB	1.55 dB
$\epsilon_{\text{PMBM}}^{\text{R}}$	-10.82 %	-5.91 %
$\sigma_{\text{PMBM}}^{\text{R}}$	5.01 %	2.12 %

while, in Fig. 5, the target T_2 is placed in $\mathbf{X}_2 = [d/2, y_2]^T$ with $-2.5 \leq y_2 \leq 2.5$ m and 0.25 m increments, thus crossing the LOS path in the middle. For symmetry reasons, the results depend only on the distance $|y_2|$ from the LOS line.

In these figures, we compare the results of the MBM and PMBM against the ones of the EM simulations obtained with Feko using vertically and horizontally polarized sources (i.e., Feko V. pol. and H. pol., respectively). For these simulations, a 2-D PEC surface has been used as target instead of the absorbing one defined in Section II for MBM and PMBM, but with the same physical dimensions adopted for Fig. 1. Thus, targets T_1 and T_2 have the same size $c_1 = c_2 = 0.55$ m and height $h_1 = h_2 = 1.80$ m, while $H = 0.90$ m and $d = 5.0$ m.

The average error ϵ_{MBM} (and ϵ_{PMBM}) between the extra attenuation values predicted by the MBM (and PMBM) and simulated by the Feko PEC (V. pol.) is also summarized in Table I. The corresponding standard deviation values σ_{MBM} and σ_{PMBM} are shown as well. Table I also shows the average errors as percentages of the total path-loss attenuation $\epsilon_{\text{MBM}}^{\text{R}}$ and $\epsilon_{\text{PMBM}}^{\text{R}}$, and the standard deviation, namely $\sigma_{\text{MBM}}^{\text{R}}$ and $\sigma_{\text{PMBM}}^{\text{R}}$. Notice that MBM model can be effectively used to predict the total path-loss values although these are underestimated compared with the Feko simulations.

In Fig. 4, the target moves along the LOS positions. The average errors are $\epsilon_{\text{MBM}} = -2.07$ dB and $\epsilon_{\text{PMBM}} = -8.69$ dB, respectively, while the corresponding standard deviations are $\sigma_{\text{MBM}} = 3.36$ dB and $\sigma_{\text{PMBM}} = 4.37$ dB as well. Assuming the total path-loss attenuation values, the average percentage relative errors are $\epsilon_{\text{MBM}}^{\text{R}} = -2.44\%$ and $\epsilon_{\text{PMBM}}^{\text{R}} = -10.82\%$. The difference between the values predicted by the MBM (and PMBM) model and the Feko simulations are due to the fact that the former employs absorbing targets and neglects any polarization, while the latter exploits metallic plates and includes the polarization effects. The positions with larger mismatches (i.e., up to $5 \div 6$ dB) are visible in the right of Fig. 4 where the target T_2 is very close to the receiver and the metallic nature of the PEC is more evident. Even if some positions of Fig. 4 show some relevant differences between MBM and Feko results, the general trend is maintained. Finally, it is also worth noticing the strong mismatches between vertically and horizontally polarized results obtained with Feko.

In Fig. 5, the target T_2 now moves along the orthogonal line that crosses the LOS in the middle at $x_2 = d/2 = 2.5$ m. The predicted MBM values corresponding to the positions across the LOS are very close to the Feko ones with a maximum error of $1 \div 2$ dB. Therefore, the errors σ_{MBM} and $\sigma_{\text{MBM}}^{\text{R}}$ are smaller than the corresponding ones along the LOS. In particular, $\epsilon_{\text{MBM}} = -0.98$ dB, $\sigma_{\text{MBM}} = 0.74$ dB, $\epsilon_{\text{MBM}}^{\text{R}} = -1.50\%$ and $\sigma_{\text{MBM}}^{\text{R}} = 1.11\%$, considering all positions across the LOS line. On the contrary, in the same figure, it is also apparent that the PMBM predictions are less accurate than the MBM ones with a maximum error in the order of $4 \div 5$ dB with respect to the Feko simulations. In particular, it is $\epsilon_{\text{PMBM}} = -4.00$ dB, $\sigma_{\text{PMBM}} = 1.55$ dB, $\epsilon_{\text{PMBM}}^{\text{R}} = -5.91\%$, and $\sigma_{\text{PMBM}}^{\text{R}} = 2.12\%$.

Fig. 5 shows also the results corresponding to the SBM/PSBM models for the single target T_1 that are superimposed to other ones. In fact, when the target T_2 moves away from the LOS path, the effects due to this target vanish, while the extra attenuation can be well predicted using only the single-target body models for T_1 .

B. Model Optimization and Experimental Setup

DFL and, in general, HPS systems, rely on several calibration steps that include off-line measurements stages to collect ground-truth measurements of RSS or CQI signals. Almost all localization systems, e.g., [6], [9], [43], [44], [47], assume free-space attenuation and propagation effects in the empty scenario as known (i.e., measured during initialization and updated periodically). On the contrary, superimposed body effects are typically not known or require either modeling or time-consuming calibration. Extra attenuation is thus obtained by compensating the background effects on the full attenuation. Thus, detection algorithms, e.g., based on finger-printing approaches [6] or statistical methods [43], [44], require also the presence of the target(s) in known locations, namely landmark points, to perform RF measurements with target(s) inside the monitored area. These steps are very time-consuming and error-prone since each RF node needs to perform noisy RSS signal measurements for the assessment of body-induced alterations of the radio propagation with the target(s) placed in selected landmarks (i.e., 2–4 landmarks/sqm depending on the network placement). In addition, systematic errors can be also introduced in the experimental setup during target positioning. Moreover, modifications of the environment involve frequent recalibration steps to maintain a good level of localization accuracy. In what follows, we investigate the use of the MBMs of Section III optimized to replace, or simplify, such calibration steps [10].

Model optimization, or tuning, is performed during an initial calibration stage to estimate both MBM and PMBM model parameters, i.e., the geometrical sizes \mathbf{c} and \mathbf{h} . We thus collect a small set of measurements in selected landmark points [10]: these are used to tune the geometrical parameters, i.e., the *EM-equivalent* height h_n and width $c_n \in [a_n, b_n]$ of the n th deployed subject. Using these optimized parameters, MBM and PMBM models can be finally adopted to predict body effects at arbitrary positions, replacing conventional calibration stages [6].

RSS data have been collected in a large hall by using two IEEE 802.15.4-compliant radio devices based on the NXP JN5148 system-on-chip (SoC) [63], which are employed as transceiver (TX/RX) nodes. Link geometry is $H = 0.9$ m and $d = 5.0$ m for all cases. Each device has a nominal EIRP equal to 0 dBm and it is equipped with a vertical monopole antenna having $G_R = 2$ dBi. Every device is programmed to send IEEE 802.15.4 standard-compliant frames at frequency $f_c = 2.48$ GHz corresponding to the IEEE 802.15.4 channel #26 [61]. Each receiver decodes the IEEE 802.15.4 frames to extract measurements of the RSS, namely the digital RSS Indicator (RSSI) with 8 bit resolution [64] and 1 dB quantization. Two sets of measurements have been gathered: the first dataset, acquired in the empty scenario, has been used to compute the reference values μ_0 and σ_0^2 , whereas the second one has been recorded with two targets placed in the link area and moving concurrently. The second dataset has been used to measure $\mu_1(\mathbf{X})$ and $\sigma_1^2(\mathbf{X})$ for some known landscape positions \mathbf{X} . In particular, the subject T_1 was placed at $\mathbf{X}_1 = [2.5, 0.0]^T$ from the transmitter, and the second subject T_2 covered four different positions, $\mathbf{X}_2 = [x_2, 0.0]^T$, at distances $x_2 = 3.0$ m, $x_2 = 3.5$ m, $x_2 = 4.0$ m, and $x_2 = 4.5$ m. These locations have been used to optimize the EM-equivalent geometrical dimensions c_1 , c_2 , h_1 , and h_2 of the individual subjects using a nonlinear least squares (NLS) approach similar to the one shown in [65] and [10]. The optimization is iterative and uses the nominal (i.e., the physical) size of the targets as initial inputs, namely $c_1 = c_2 = 0.4$ m and $h_1 = h_2 = 1.7$ m (neglecting head). Optimized EM-equivalent target sizes are $c_1 = c_2 = 0.25$ m and $h_1 = h_2 = 1.35$ m. The EM-equivalent size is about 20% ÷ 40% smaller than the physical size of the target as also shown in [36]; this might be due to the fact that body-induced extra attenuations are mostly due to torso and legs, while head and arms effects are negligible, although they are responsible for some small RSSI fluctuations.

C. Model Comparison With Measurements

Based on the experimental setup described in the previous section, we compare in Fig. 6 the predicted extra attenuation $E_{\chi, \Delta \mathbf{X}}[A_{\text{dB}}^{(1,2)}(\mathbf{X}|\Delta \mathbf{X}, \chi, \Lambda)]$ using the MBM and PMBM models against the field measurements. RSSI measurements, averaged over a period of 1 minute, are shown in Fig. 6 as red cross markers. Horizontal error bars are also depicted to account for positioning inaccuracies (± 0.25 m) during the tests, while vertical bars and dots indicate the max-min and mean RSSI values, respectively. The solid lines show the predicted MBM (black line) and PMBM (blue line) extra attenuations using the optimized EM-equivalent parameters. For prediction, we consider two knife edges orthogonally placed along the LOS path in fixed positions ($B = 0$) with no rotation. In particular, subject T_1 , initially placed at $\mathbf{X}_1 = [0.5, 0.0]^T$ from the TX, covers a distance of 1.5 m with 0.5 m increments in the direction of the RX (thus stopping at $\mathbf{X}_1 = [2.0, 0.0]^T$ from the TX). Subject T_2 moves toward the

receiver with 0.5 m increments and stops at 0.5 m from the RX device.

To highlight the comparative analysis with measurements, we neglect the residual stochastic body-induced multipath fading terms by assuming $\Delta\sigma_c^2 = 0$ dB and $\Delta h_C = 0$ dB so that (21) reduces to $-\Delta\mu(\mathbf{X}) = E_{\chi, \Delta \mathbf{X}}[A_{\text{dB}}^{(1,2)}(\mathbf{X}|\Delta \mathbf{X}, \chi, \Lambda)] = A_{\text{dB}}^{(1,2)}(\mathbf{X}|\Lambda)$. Besides MBM and PMBM models, based on the discussion in Section II-E, for the same settings, we have also compared the additive hypothesis, namely $A_{\text{dB}}^{(1,2)} = A_{\text{dB}}^{(1)} + A_{\text{dB}}^{(2)}$. In particular, the additive SBM approximation is depicted in black dashed lines; in this case, the predicted extra attenuation reduces to $-\Delta\mu(\mathbf{X}) = E_{\chi_1, \Delta \mathbf{X}_1}[A_{\text{dB}}^{(1)}(\mathbf{X}|\Delta \mathbf{X}, \chi, \Lambda)] + E_{\chi_2, \Delta \mathbf{X}_2}[A_{\text{dB}}^{(2)}(\mathbf{X}|\Delta \mathbf{X}, \chi, \Lambda)] = A_{\text{dB}}^{(1)}(\mathbf{X}|\Lambda) + A_{\text{dB}}^{(2)}(\mathbf{X}|\Lambda)$ where $A_{\text{dB}}^{(1)}(\mathbf{X}|\Lambda)$ and $A_{\text{dB}}^{(2)}(\mathbf{X}|\Lambda)$ follow the SBM model described in Section II-A and use the same optimized EM-equivalent target size used for the MBM model.

In Fig. 6, the shaded areas indicate the ± 1 dB uncertainty zone around the mean values predicted by the MBM (i.e., beige area) and the additive SBM (i.e., light blue area) models. Assuming Gaussian distributions, for each uncertainty zone, 68.3% of the related events fall inside each shaded area.

The discrepancies between the proposed models and the measurements may be large for some target positions, configurations, and scenarios. This is due to some approximations adopted for the MBM/PMBM, SBM/PSBM, and additive SBM models that have been summarized in Section II-F. In addition to the above, there are also some noisy effects introduced during the RSS measurement process. First, the human bodies are never fixed in specific positions but, while standing, they perform both voluntary and/or involuntary movements around the nominal position due to movements of the legs, torso, arms, and head. This unavoidable experimental fact can introduce variations in the order of 2 ÷ 3 dB for the single-target case [46]. Due to the complex structure of the human body and the difficulties to measure its true position [46], [65], the nominal (i.e., measured) position of the target is only approximately known with an error in the order of 10 ÷ 15 cm. Second, measurements are taken in real scenarios where some unavoidable multipath effects are present. These effects are modeled as a lognormal distributed noise even if this is an approximated behavior [59]. Finally, the RSS values measured by the IEEE 802.15.4 radio devices are corrupted by measurement noise and nonlinearity effects [64] that cause further measurement errors in the order of 0.5 ÷ 1.5 dB, depending on the adopted device. Offset errors can be compensated due to the fact that the extra attenuation is measured with respect to the free-space scenarios but nonlinearity and quantization cannot.

In Fig. 6, the MBM and PMBM predictions track the average RSSI measurements with an average error of about 4 dB and 6 dB, respectively. Notice that most of the mismatches between the models and the measurements are observed in correspondence to one of the targets (or both) near the transmitter or the receiver. In such cases, the RSSI measurements

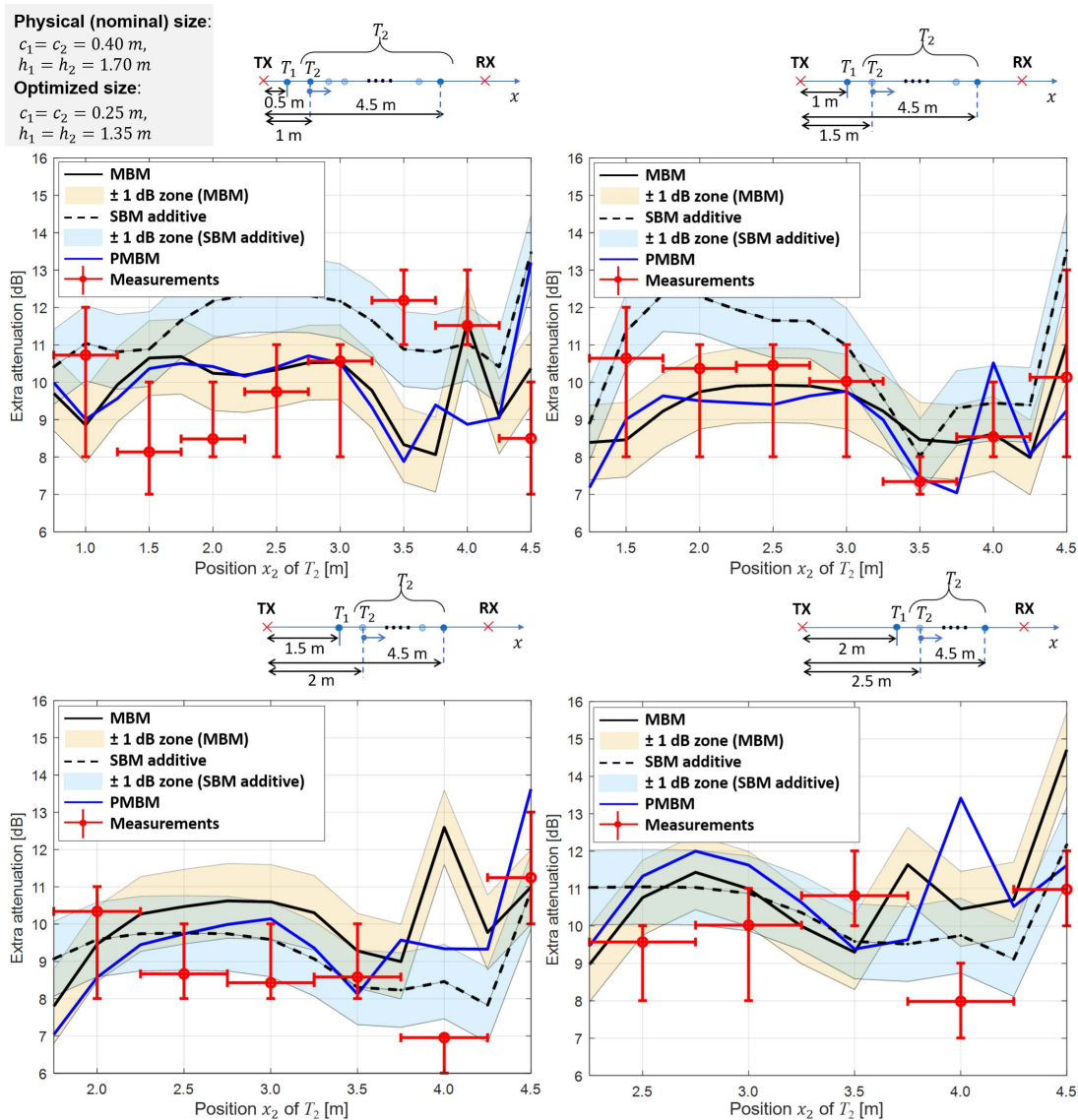


Fig. 6. Predicted extra attenuation values using MBM (black line), PMBM (blue line), and additive SBM (black dashed line) against the measured ones (red cross, with vertical and horizontal error bars) considering four motion scenarios featuring $N = 2$ targets. The ± 1 dB uncertainty zones are shown around the additive SBM (light blue area) and the MBM (beige area) results. Each scenario is depicted in the corresponding subfigure.

might also be affected by larger communication errors due to the increase of body-induced extra attenuation. Fluctuations of RSSI around the average value cause residual stochastic terms that can be quantified as a variance term $\Delta\sigma_C^2 \simeq 3$ dB and negligible mean $\Delta h_C \simeq 0$ dB; these are mostly due to voluntary/involuntary movements of the bodies around their nominal positions. The additive SBM model is generally less effective compared with MBM, particularly when the mixed terms in (14), caused by the interacting targets T_1 and T_2 , could not be neglected. This is, for example, the case when both subjects equally contribute to the extra attenuation.

V. CONCLUSION

Based on the EM scalar diffraction theory, this article proposes for the first time an *ad hoc* physical–statistical

model to describe the fluctuations of the radio signal caused by the presence of an arbitrary number of targets between the transmitter and the receiver. The analytical model has been specifically tuned and optimized to predict the effects of multiple bodies placed near the link area. Therefore, it is instrumental to DFL applications and HPS, including people access monitoring and counting. The model results have been validated experimentally by some field tests using real industrial wireless devices and EM simulations as well, for comparative analysis. The proposed MBM model is able to predict the RSS measurements accounting for the size, orientation, small movements, and positions of the targets. It overcomes also some restrictions of the existing MBMs based on the linear superposition of the subject effects, thus showing improved prediction accuracy.

APPENDIX

In what follows, we resort to a formulation of (15) similar to that used in (11). It is

$$\begin{aligned}
(-1)^N \frac{E^{(1,2,\dots,N)}}{E_0} &= -1 + \sum_{n=1}^N \frac{E^{(n)}}{E_0} - \sum_{n=1}^{N-1} \sum_{m=n+1}^N \frac{E^{(n,m)}}{E_0} \\
&+ \sum_{n=1}^{N-2} \sum_{m=n+1}^{N-1} \sum_{k=m+1}^N \frac{E^{(n,m,k)}}{E_0} + \dots + \\
&+ \tilde{\Psi}(S_1, \dots, S_N) \quad (23)
\end{aligned}$$

with the last term $\tilde{\Psi}(S_1, \dots, S_N)$ given by

$$\begin{aligned}
&\tilde{\Psi}(S_1, \dots, S_N) \\
&= \left(\frac{j}{2}\right)^N \int_{S_1} \int_{S_2}, \dots, \int_{S_N} \\
&\quad \times \frac{d d_{1,2} d_{2,3}, \dots, d_{N-1,N}}{(d_1 + d_{1,2})(d_{1,2} + d_{2,3}), \dots, (d_{N-1,N} + d_N)} \\
&\quad \cdot \exp\left\{-j\frac{\pi}{2}(u_1^2 + u_2^2 + \dots + u_N^2 - 2\alpha_{1,2}u_1u_2 \dots \right. \\
&\quad \quad \left. + 2\alpha_{N-1,N}u_{N-1}u_N)\right\} du_1 du_2, \dots, du_N \\
&\quad \cdot \exp\left\{-j\frac{\pi}{2}(v_1^2 + v_2^2 + \dots + v_N^2 - 2\alpha_{1,2}v_1v_2 \dots \right. \\
&\quad \quad \left. + 2\alpha_{N-1,N}v_{N-1}v_N)\right\} dv_1 dv_2, \dots, dv_N. \quad (24)
\end{aligned}$$

The variables $u_1, \dots, u_N, v_1, \dots, v_N$ are obtained from the corresponding local coordinates $\xi_1, \dots, \xi_N, \zeta_1, \dots, \zeta_N$ by using, for each n th term, the following substitution rules: $u_n = \xi_n(\sqrt{2}/R_n)$ and $v_n = \zeta_n(\sqrt{2}/R_n)$. The constant terms R_n and $\alpha_{n,n+1}$ are related to the wavelength λ and the geometric positions of the knife edges with respect to the LOS path. The terms R_n are similar to the Fresnel's radius R for the single-target case. These constants are given by

$$\frac{1}{R_n^2} = \begin{cases} \frac{1}{\lambda} \left(\frac{1}{d_1} + \frac{1}{d_{12}} \right), & \text{for } n = 1 \\ \frac{1}{\lambda} \left(\frac{1}{d_{n-1,n}} + \frac{1}{d_{n,n+1}} \right), & \text{for } n = 2, \dots, N-1 \\ \frac{1}{\lambda} \left(\frac{1}{d_N} + \frac{1}{d_{N-1,N}} \right), & \text{for } n = N \end{cases} \quad (25)$$

while coefficients $\alpha_{n,n+1}$ are defined, for $n = 1, \dots, N-1$, as

$$\alpha_{n,n+1} = \frac{R_n R_{n+1}}{\lambda d_{n,n+1}}. \quad (26)$$

For the single-target case, it is $R_1 = R$, while all coefficients $\alpha_{n,n+1}$ vanish. In addition, it is trivial to verify that (11) simply reduces to (4), while (23) simplifies to (5). For $N = 2$, (11) reduces to the dual-target case (13) and proves the results [8], [10] exploited for DFL applications.

REFERENCES

- [1] V. Petrov *et al.*, "When IoT keeps people in the loop: A path towards a new global utility," *IEEE Commun. Mag.*, vol. 57, no. 1, pp. 114–121, Jan. 2019.
- [2] N. Dalal and B. Triggs, "Histograms of oriented gradients for human detection," in *Proc. IEEE Comput. Soc. Conf. Comput. Vis. Pattern Recognit.*, Jun. 2005, vol. 1, no. 1, pp. 886–893.
- [3] Y. Benezeth, H. Laurent, B. Emile, and C. Rosenberger, "Towards a sensor for detecting human presence and characterizing activity," *Energy Buildings*, vol. 43, nos. 2–3, pp. 305–314, Feb./Mar. 2011.
- [4] B. Choi, C. Meriçli, J. Biswas, and M. Veloso, "Fast human detection for indoor mobile robots using depth images," in *Proc. IEEE Int. Conf. Robot. Autom.*, May 2013, pp. 1108–1113.
- [5] M. Youssef, M. Mah, and A. Agrawala, "Challenges: Device-free passive localization for wireless environments," in *Proc. 13th Annu. ACM Int. Conf. Mobile Comput. Netw. (MobiCom)*, 2007, pp. 222–229.
- [6] S. Savazzi, S. Sigg, M. Nicoli, V. Rampa, S. Kianoush, and U. Spagnolini, "Device-free radio vision for assisted living: Leveraging wireless channel quality information for human sensing," *IEEE Signal Process. Mag.*, vol. 33, no. 2, pp. 45–58, Mar. 2016.
- [7] J. Wilson and N. Patwari, "Radio tomographic imaging with wireless networks," *IEEE Trans. Mobile Comput.*, vol. 9, no. 5, pp. 621–632, May 2010.
- [8] M. Nicoli, V. Rampa, S. Savazzi, and S. Schiaroli, "Device-free localization of multiple targets," in *Proc. 24th Eur. Signal Process. Conf. (EUSIPCO)*, Aug. 2016, pp. 738–742.
- [9] J. Wang *et al.*, "E-HIPA: An energy-efficient framework for high-precision multi-target-adaptive device-free localization," *IEEE Trans. Mobile Comput.*, vol. 16, no. 3, pp. 716–729, Mar. 2017.
- [10] V. Rampa, M. Nicoli, C. Manno, and S. Savazzi, "EM model-based device-free localization of multiple bodies," *Sensors*, vol. 21, no. 5, pp. 1–22, 2021.
- [11] S. Depatla, A. Muralidharan, and Y. Mostofi, "Occupancy estimation using only WiFi power measurements," *IEEE J. Sel. Areas Commun.*, vol. 33, no. 7, pp. 1253–1264, Jul. 2015.
- [12] S. Savazzi, S. Kianoush, and V. Rampa, "A dynamic Bayesian network approach for device-free radio vision: Modeling, learning and inference for body motion recognition," in *Proc. IEEE Int. Conf. Acoust., Speech Signal Process. (ICASSP)*, Mar. 2016, pp. 6265–6269.
- [13] W. Wang, A. X. Liu, M. Shahzad, K. Ling, and S. Lu, "Understanding and modeling of WiFi signal based human activity recognition," in *Proc. 21st Annu. Int. Conf. Mobile Comput. Netw.*, Sep. 2015, pp. 65–76.
- [14] S. Kianoush, S. Savazzi, F. Vicentini, V. Rampa, and M. Giussani, "Device-free RF human body fall detection and localization in industrial workplaces," *IEEE Internet Things J.*, vol. 4, no. 2, pp. 351–362, Apr. 2017.
- [15] Z. Talebpoor and A. Martinoli, "Adaptive risk-based replanning for human-aware multi-robot task allocation with local perception," *IEEE Robot. Autom. Lett.*, vol. 4, no. 4, pp. 3790–3797, Oct. 2019.
- [16] A. Montanari, S. Nawaz, C. Mascolo, and K. Sailer, "A study of Bluetooth low energy performance for human proximity detection in the workplace," in *Proc. IEEE Int. Conf. Pervasive Comput. Commun. (PerCom)*, Mar. 2017, pp. 90–99.
- [17] K. Woyach, D. Puccinelli, and M. Haenggi, "Sensorless sensing in wireless networks: Implementation and measurements," in *Proc. 4th Int. Symp. Modelling Optim. Mobile, Ad Hoc Wireless Netw.*, Apr. 2006, pp. 1–8.
- [18] N. Patwari and J. Wilson, "RF sensor networks for device-free localization: Measurements, models, and algorithms," *Proc. IEEE*, vol. 98, no. 11, pp. 1961–1973, Nov. 2010.
- [19] M. Seifeldin, A. Saeed, A. E. Kosba, A. El-Keyi, and M. Youssef, "Nuzzer: A large-scale device-free passive localization system for wireless environments," *IEEE Trans. Mobile Comput.*, vol. 12, no. 7, pp. 1321–1334, Jul. 2013.
- [20] A. Saeed, A. E. Kosba, and M. Youssef, "Ichnaea: A low-overhead robust WLAN device-free passive localization system," *IEEE J. Sel. Topics Signal Process.*, vol. 8, no. 1, pp. 5–15, Feb. 2014.
- [21] S. Obayashi and J. Zander, "A body-shadowing model for indoor radio communication environments," *IEEE Trans. Antennas Propag.*, vol. 46, no. 6, pp. 920–927, Jun. 1998.
- [22] F. Villanese, N. E. Evans, and W. G. Scanlon, "Pedestrian-induced fading for indoor channels at 2.45, 5.7 and 62 GHz," in *Proc. 52nd Veh. Technol. Conf.*, Sep. 2000, pp. 43–48.
- [23] J. E. Brittain, "Albert Hoyt Taylor [Scanning the Past]," *Proc. IEEE*, vol. 82, no. 6, p. 958, Jun. 1994.
- [24] K. Furutsu, "On the theory of radio wave propagation over inhomogeneous earth," *J. Res. NBS—D, Radio Propag.*, vol. 67D, no. 1, pp. 39–62, Jan./Feb. 1963.
- [25] L. E. Vogler, "An attenuation function for multiple knife-edge diffraction," *Radio Sci.*, vol. 17, no. 6, pp. 1541–1546, 1982.
- [26] H. Mokhtari and P. Lazaridis, "Comparative study of lateral profile knife-edge diffraction and ray tracing technique using GTD in urban environment," *IEEE Trans. Veh. Technol.*, vol. 48, no. 1, pp. 255–261, Jan. 1999.

- [27] C. Tzaras and S. R. Saunders, "Comparison of multiple-diffraction models for digital broadcasting coverage prediction," *IEEE Trans. Broadcast.*, vol. 46, no. 3, pp. 221–226, Sep. 2000.
- [28] D. B. Smith, D. Miniutti, T. A. Lamahewa, and L. W. Hanlen, "Propagation models for body-area networks: A survey and new outlook," *IEEE Antennas Propag. Mag.*, vol. 55, no. 5, pp. 97–117, Oct. 2013.
- [29] G. Koutitas, "Multiple human effects in body area networks," *IEEE Antennas Wireless Propag. Lett.*, vol. 9, pp. 938–941, Sep. 2010.
- [30] A. D. C. de Queiroz and L. C. Trintinalia, "An analysis of human body shadowing models for ray-tracing radio channel characterization," in *Proc. SBMO/IEEE MTT-S Int. Microw. Optoelectron. Conf. (IMOC)*, Nov. 2015, pp. 1–5.
- [31] N. Cho, J. Yoo, S.-J. Song, J. Lee, S. Jeon, and H.-J. Yoo, "The human body characteristics as a signal transmission medium for intrabody communication," *IEEE Trans. Microw. Theory Techn.*, vol. 55, no. 5, pp. 1080–1086, May 2007.
- [32] C. Andreu, S. Castelló-Palacios, C. Garcia-Pardo, A. Fornes-Leal, A. Vallés-Lluch, and N. Cardona, "Spatial in-body channel characterization using an accurate UWB phantom," *IEEE Trans. Microw. Theory Techn.*, vol. 64, no. 11, pp. 3995–4002, Nov. 2016.
- [33] Y. I. Nechayev, P. S. Hall, and Z. H. Hu, "Characterisation of narrowband communication channels on the human body at 2.45 GHz," *IET Microw., Antennas Propag.*, vol. 4, no. 6, pp. 722–732, 2010.
- [34] A. Fort, J. Ryckaert, C. Desset, P. De Doncker, P. Wambacq, and L. Van Biesen, "Ultra-wideband channel model for communication around the human body," *IEEE J. Sel. Areas Commun.*, vol. 24, no. 4, pp. 927–933, Apr. 2006.
- [35] L. Liu, P. De Doncker, and C. Oestges, "Fading correlation measurement and modeling on the front side of a human body," in *Proc. IEEE 3rd Eur. Conf. Antennas Propag.*, Mar. 2009, pp. 969–973.
- [36] M. Ghaddar, L. Talbi, T. A. Denidni, and A. Sebak, "A conducting cylinder for modeling human body presence in indoor propagation channel," *IEEE Trans. Antennas Propag.*, vol. 55, no. 11, pp. 3099–3103, Nov. 2007.
- [37] B. R. Hamilton, X. Ma, R. J. Baxley, and S. M. Matechik, "Propagation modeling for radio frequency tomography in wireless networks," *IEEE J. Sel. Topics Signal Process.*, vol. 8, no. 1, pp. 55–65, Feb. 2014.
- [38] H. Yigitler and R. Jantti, "Experimental accuracy assessment of radio tomographic imaging methods," in *Proc. IEEE Int. Conf. Pervasive Comput. Commun. Workshops (PerCom Workshops)*, Mar. 2016, pp. 1–6.
- [39] A. Eleryan, M. Elsabagh, and M. Youssef, "Synthetic generation of radio maps for device-free passive localization," in *Proc. IEEE Global Telecommun. Conf.*, Dec. 2011, pp. 1–5.
- [40] B. Kibret, A. K. Teshome, and D. T. H. Lai, "Characterizing the human body as a monopole antenna," *IEEE Trans. Antennas Propag.*, vol. 63, no. 10, pp. 4384–4392, Oct. 2015.
- [41] K. I. Ziri-Castro, W. G. Scanlon, and N. E. Evans, "Prediction of variation in MIMO channel capacity for the populated indoor environment using a radar cross-section-based pedestrian model," *IEEE Trans. Wireless Commun.*, vol. 4, no. 3, pp. 1186–1194, May 2005.
- [42] M. Yokota, K. Shiya, Y. Ohta, and T. Fujii, "Propagation loss properties in case human bodies exist between transmitter and receiver," in *Proc. IEEE Int. Symp. Antennas Propag.*, Oct./Nov. 2012, pp. 343–346.
- [43] Y. Guo, K. Huang, N. Jiang, X. Guo, Y. Li, and G. Wang, "An exponential-Rayleigh model for RSS-based device-free localization and tracking," *IEEE Trans. Mobile Comput.*, vol. 14, no. 3, pp. 484–494, Mar. 2015.
- [44] O. Kaltiokallio, H. Yigitler, and R. Jantti, "A three-state received signal strength model for device-free localization," *IEEE Trans. Veh. Technol.*, vol. 66, no. 10, pp. 9226–9240, Oct. 2017.
- [45] M. Mohamed, M. Cheffena, A. A. Moldsvor, and F. P. Fontan, "Physical-statistical channel model for off-body area network," *IEEE Antennas Wireless Propag. Lett.*, vol. 16, pp. 1516–1519, Jan. 2017.
- [46] V. Rampa, G. G. Gentili, S. Savazzi, and M. D'Amico, "EM models for passive body occupancy inference," *IEEE Antennas Wireless Propag. Lett.*, vol. 16, pp. 2517–2520, Jul. 2017.
- [47] P. Hillyard and N. Patwari, "Never use labels: Signal strength-based Bayesian device-free localization in changing environments," *IEEE Trans. Mobile Comput.*, vol. 19, no. 4, pp. 894–906, Apr. 2020.
- [48] V. Rampa, S. Savazzi, M. D'Amico, and G. G. Gentili, "Dual-target body model for device-free localization applications," in *Proc. IEEE-APS Topical Conf. Antennas Propag. Wireless Commun. (APWC)*, Sep. 2019, pp. 181–186.
- [49] S. W. Lee, "Path integrals for solving some electromagnetic edge diffraction problems," *J. Math. Phys.*, vol. 19, no. 6, pp. 1414–1422, Jun. 1978.
- [50] G. D. Durgin, "The practical behavior of various edge-diffraction formulas," *IEEE Antennas Propag. Mag.*, vol. 51, no. 3, pp. 24–35, Jun. 2009.
- [51] J. Deygout, "Correction factor for multiple knife-edge diffraction," *IEEE Trans. Antennas Propag.*, vol. 39, no. 8, pp. 1256–1258, Aug. 1991.
- [52] V. Rampa, S. Savazzi, M. Nicoli, and M. D'Amico, "Physical modeling and performance bounds for device-free localization systems," *IEEE Signal Process. Lett.*, vol. 22, no. 11, pp. 1864–1868, Nov. 2015.
- [53] R. J. Luebbers, "Finite conductivity uniform GTD versus knife edge diffraction in prediction of propagation path loss," *IEEE Trans. Antennas Propag.*, vol. TAP-32, no. 1, pp. 70–76, Jan. 1984.
- [54] M. Ghaddar, L. Talbi, T. A. Denidni, and A. Charbonneau, "Modeling human body effects for indoor radio channel using UTD," in *Proc. IEEE Can. Conf. Electr. Comput. Eng.*, May 2004, pp. 1357–1360.
- [55] E. Reusens et al., "Path loss models for wireless communication channel along arm and torso: Measurements and simulations," in *Proc. IEEE Antennas Propag. Soc. Int. Symp.*, Jun. 2007, pp. 345–348.
- [56] B. A. Davis and G. S. Brown, "Diffraction by a randomly rough knife edge," *IEEE Trans. Antennas Propag.*, vol. 50, no. 12, pp. 1769–1778, Dec. 2002.
- [57] *Propagation Data and Prediction Methods for the Planning of Indoor Radiocommunication Systems and Radio Local Area Networks in the Frequency Range 900 MHz to 100 GHz, P Series Radiowave Propagation*, document ITU-R P.1238-10, Aug. 2019.
- [58] S. Savazzi, M. Nicoli, F. Carminati, and M. Riva, "A Bayesian approach to device-free localization: Modeling and experimental assessment," *IEEE J. Sel. Topics Signal Process.*, vol. 8, no. 1, pp. 16–29, Feb. 2014.
- [59] A. J. Coulson, A. G. Williamson, and R. G. Vaughan, "A statistical basis for lognormal shadowing effects in multipath fading channels," *IEEE Trans. Commun.*, vol. 46, no. 4, pp. 494–502, Apr. 1998.
- [60] A. Z. Elsherbeni, P. Nayeri, and C. Reddy, *Antenna Analysis and Design Using FEKO Electromagnetic Simulation Software* (The ACES Series on Computational Electromagnetics and Engineering). Rijeka, Croatia: SciTech, 2014.
- [61] *IEEE Standard for Local and Metropolitan Area Networks—Part 15.4: Low-Rate Wireless Personal Area Networks (LR-WPANs) Amendment 1: MAC Sublayer*, IEEE Standard 802.15.4e-2012, (Amendment to IEEE Standard 802.15.4-2011), Apr. 2012, pp. 1–225.
- [62] S. Savazzi, V. Rampa, F. Vicentini, and M. Giussani, "Device-free human sensing and localization in collaborative human-robot workspaces: A case study," *IEEE Sensors J.*, vol. 16, no. 5, pp. 1253–1264, Mar. 2016.
- [63] NXP Lab., Scotland, U.K. (2010). *Data-Sheet JN-DS-JN5148-001: IEEE 802.15.4 Wireless Microcontroller JN5148-001*. [Online]. Available: https://www.nxp.com/docs/en/brochure/JN5148_PB_1v4.pdf
- [64] Y. Chen and A. Terzis, "On the mechanisms and effects of calibrating RSSI measurements for 802.15.4 radios," in *Proc. Eur. Conf. Wireless Sensor Netw. (EWSN)*, 2010, pp. 256–271.
- [65] V. Rampa, S. Savazzi, and S. Kianoush, "Physical model-based calibration for device-free radio localization and motion tracking," in *Proc. IEEE-APS Topical Conf. Antennas Propag. Wireless Commun. (APWC)*, Sep. 2019, pp. 353–358.



Vittorio Rampa (Member, IEEE) received the Laurea degree (Hons.) in electronics engineering from the Politecnico di Milano, Milan, Italy, in 1984.

In 1986, he joined the Consiglio Nazionale delle Ricerche (CNR) of Italy, Milan, as a Researcher. From 1999 to 2014, he was an Adjunct Professor with the Politecnico di Milano, where he taught courses on software-defined radios and radio localization systems. In 2001, he became a Senior Researcher with the Institute of Electronics, Computer and Telecommunication Engineering (IEIIT). He has coauthored more than 95 scientific publications. His main research interests include signal processing algorithms and architectures for wireless communications, machine and deep learning algorithms for sensor networks, radio vision models, and algorithms and systems.



Gian Guido Gentili was born in Turin, Italy, in 1961. He received the Laurea degree in electronics engineering from the Politecnico di Milano, Milan, Italy, in 1987.

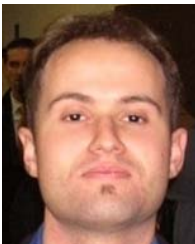
In 1989, he joined the Consiglio Nazionale delle Ricerche (CNR), Center for Space Telecommunications, as a Researcher, where in 2001, he became a Senior Researcher. He became an Associate Professor with the Politecnico di Milano in 2002. He was a Visiting Scholar at the Politecnica de Madrid in 1993 and 1995. He is responsible for the

Electromagnetics Laboratory *Wavelab*, Politecnico di Milano. His research interests include numerical method for electromagnetics (finite elements, method of moments (MoM), and mode matching), antennas and feed systems for terrestrial and space applications, microwave passive devices and filters, and plasmonics.



Michele D'Amico (Senior Member, IEEE) graduated from Politecnico di Milano, Milan, Italy, in 1990, and the Ph.D. degree in mathematics from the University of Essex, Colchester, U.K., in 1997.

Since 2002, he has been an Associate Professor in applied electromagnetics at DEIB (Politecnico di Milano). Research activities include antennas, electromagnetic wave propagation in the troposphere at frequencies above 10 GHz, and radarmeteorology. He has several patents on antennas and has authored or coauthored more than 130 articles published in international journals or conference proceedings.



Stefano Savazzi (Member, IEEE) received the M.Sc. degree and the Ph.D. degree (Hons.) in ICT from the Politecnico di Milano, Milan, Italy, in 2004 and 2008, respectively.

In 2012, he joined the Institute of Electronics, Computer and Telecommunication Engineering (IEIIT), Consiglio Nazionale delle Ricerche (CNR), as a Researcher. He has coauthored over 100 scientific publications. His current research interests include distributed signal processing, learning and networking aspects for the Internet of

Things, and radio vision and localization.

Dr. Savazzi received the Dimitris N. Chorafas Foundation Award in 2008. He is serving as Associate Editor for *Frontiers in Communications and Networks* and a Topic Editor for *Sensors* (MDPI).